INSTITUTE OF PHYSICS PUBLISHING NANOTECHNOLOGY
Nanotechnology **16** (2005) S562–S574 doi:10.1088/0957-4484/16/7/034

Predictive control of crystal size distribution in protein crystallization

Dan Shi, Prashant Mhaskar, Nael H El-Farra and Panagiotis D Christofides[1]

Department of Chemical Engineering, University of California, Los Angeles, CA, USA

E-mail: pdc@seas.ucla.edu

Received 16 December 2004, in final form 14 April 2005
Published 2 June 2005
Online at stacks.iop.org/Nano/16/S562

Abstract

This work focuses on the modelling, simulation and control of a batch protein crystallization process that is used to produce the crystals of tetragonal hen egg-white (HEW) lysozyme. First, a model is presented that describes the formation of protein crystals via nucleation and growth. Existing experimental data are used to develop empirical models of the nucleation and growth mechanisms of the tetragonal HEW lysozyme crystal. The developed growth and nucleation rate expressions are used within a population balance model to simulate the batch crystallization process. Then, model reduction techniques are used to derive a reduced-order moments model for the purpose of controller design. Online measurements of the solute concentration and reactor temperature are assumed to be available, and a Luenberger-type observer is used to estimate the moments of the crystal size distribution based on the available measurements. A predictive controller, which uses the available state estimates, is designed to achieve the objective of maximizing the volume-averaged crystal size while respecting constraints on the manipulated input variables (which reflect physical limitations of control actuators) and on the process state variables (which reflect performance considerations). Simulation results demonstrate that the proposed predictive controller is able to increase the volume-averaged crystal size by 30% and 8.5% compared to constant temperature control (CTC) and constant supersaturation control (CSC) strategies, respectively, while reducing the number of fine crystals produced. Furthermore, a comparison of the crystal size distributions (CSDs) indicates that the product achieved by the proposed predictive control strategy has larger total volume and lower polydispersity compared to the CTC and CSC strategies. Finally, the robustness of the proposed method (achieved due to the presence of feedback) with respect to plant-model mismatch is demonstrated. The proposed method is demonstrated to successfully achieve the task of maximizing the volume-averaged crystal size in the presence of plant-model mismatch, and is found to be robust in comparison to open-loop optimal control strategies.

(Some figures in this article are in colour only in the electronic version)

1. Introduction

Proteins play a vital role in most biological processes. In addition to constructing large-scale biological structures, such as muscle fibres, smaller protein molecules can function as antibodies, which help the immune system to destroy invading substances like viruses and bacteria, and enzymes, which can catalyse the synthesis of complex compounds, the transformation of complex substances into simpler ones, or

[1] Author to whom any correspondence should be addressed.

the generation of energy in organisms. A protein molecule is a chain of amino acids that are linked by peptide bonds formed by dehydration synthesis. Many pharmaceuticals act by binding to and blocking an active site (the active site is a region on the protein composed of some of the protein's amino acids which have a specific three-dimensional arrangement to which a molecule can bind) of a protein [45]. The three-dimensional arrangement of amino acids, especially, at the active site, determines the specific biological function of the protein molecule.

X-ray and neutron diffraction techniques are the only available methods that can be used to obtain structural information of proteins with molecular weight over 20 000. To be able to study the structure of proteins using these techniques, large protein crystals of high structural perfection, typically with diameters of several hundred microns, are needed. Extensive research studies, using model proteins, such as ferritin, insulin, haemoglobin and lysozyme, that are able to crystallize easily under normal operating conditions, have focused on growing large protein crystals of high structural perfection under various operating conditions, including low gravity [4], different pressure conditions [37], flow condition of the solution [41], purity [55], temperature [9] and concentrations of precipitants and buffers [40, 28]. In addition, numerous research studies have considered the problem of modelling of protein nucleation [17, 39] and growth [12, 26, 16]. The reader may also refer to [31, 48, 57, 54] for excellent reviews on this subject. Among these model proteins, the tetragonal form of hen egg-white (HEW) lysozyme is most popular and widely used [5]. HEW lysozyme is composed of 129 amino acids, with a molecular weight of 14 388. It is a naturally occurring enzyme, and has antibacterial activity against gram-positive bacteria.

The experimental studies not only benefit the determination of the protein structure, but also provide, through an understanding of the nucleation and growth mechanisms of protein crystallization, a way of determining the operating conditions necessary to achieve protein crystals of desired properties, which can often be expressed in the form of a desired size distribution. In the pharmaceutical industry, the size distribution of the protein crystal is a very critical variable and in many applications a predetermined, typically narrow, crystal size distribution (CSD) is necessary in order to guarantee a desired drug delivery performance.

Protein crystals intrinsically grow much more slowly than most inorganic crystals at the same supersaturation [46]. This is probably one of the reasons why it has been widely believed that implementation of advanced control algorithms is not important for growing perfect crystals in protein crystallization. However, experimental results show that even in protein crystallization processes, certain growth conditions lead to crystal defect formation (for example, the structural defect density increases when the growth rate is relatively high [35]), which necessitates appropriately choosing and employing control to maintain the desired operating conditions.

While numerous experimental studies of the nucleation and growth mechanisms of protein crystallization have been carried out, very few results on control of protein crystallization are available [38, 53, 18, 49, 20]. The feasibility and effectiveness of temperature control in protein crystallization was discussed in [47], where a series of preliminary experiments was conducted to demonstrate the ability of temperature control to manipulate the supersaturation in the protein crystallization. In [10], a method for control of nucleation in small protein solutions was developed and focused on control of a relatively smaller number of protein crystals. In [56], an experiment system was developed to control a crystallization cell, and focused on the development of the control system, including the hardware and software for measurement and communication, rather than on the control algorithm. A constant supersaturation concentration (CSC) control strategy, which can be readily implemented in practice, was developed in [51] and [20] to achieve large protein crystals, and was demonstrated to yield significant advantage in increasing the crystal size compared to the case where, for instance, the temperature in the crystallizer is held steady. For processes where the product specification is better expressed in the form of properties of the product size distribution, and as constraints on the process state variables, it is important to develop control strategies that account for these issues in the controller design. Furthermore, it is important to implement feedback control strategies (as opposed to open-loop strategies, where a pre-computed manipulated input profile is implemented for the entire duration of the batch), to mitigate the undesirable effects of modelling errors and external disturbances on the satisfaction of performance considerations and constraints during the entire batch run.

Motivated by the above considerations, this work focuses on the modelling, simulation and control of a batch protein crystallization process that is used to produce the crystals of tetragonal hen egg-white (HEW) lysozyme. First, a model is presented that describes the formation of infinitesimal-size protein crystals via nucleation and the subsequent growth of the crystals via condensation, and predicts the temporal evolution of the crystal size distribution in the size range of 0–300 μm. To this end, existing experimental data are used to develop empirical models of the nucleation and growth mechanisms of the tetragonal HEW lysozyme crystal. The developed growth and nucleation rate expressions are used within a population balance model to simulate a batch crystallization process that produces the tetragonal HEW lysozyme crystals. Then, model reduction techniques are used to derive a reduced-order moments model for the purpose of controller design. Online measurements of the solute concentration and reactor temperature are assumed to be available, and a Luenberger-type observer is developed to estimate the moments of the crystal size distribution based on the available measurements. A predictive controller, that uses the available state estimates, is designed to achieve the objective of maximizing the volume-averaged crystal size while respecting constraints on the manipulated input variables (which reflect physical limitations of control actuators) and on the process state variables (which reflect performance considerations).

2. Modelling of nucleation and growth rate of tetragonal lysozyme crystal

The formation of a single crystal can be modelled as comprising two sequential processes: crystal nucleation

and growth. Experimental studies [12, 16, 17, 25, 39] have considered various operating conditions and developed empirical models for the nucleation and growth of the tetragonal HEW lysozyme crystal. In the current study, we focus on one operating condition (fixed buffer, pH value and salt concentration; these values are selected based on the availability of experimental results), and develop an empirical model of the nucleation and growth mechanisms by using the existing experimental results available for these operating conditions. We note here that the development of the model benefits immensely from the availability of extensive experimental work on nucleation and growth of the tetragonal HEW lysozyme crystal, and aims to aid the experimental effort towards developing products with desired properties via the development of easily implementable feedback control strategies. In the remainder of this section, experimental results on the solubility, nucleation and growth of the tetragonal HEW lysozyme crystal are analysed and an empirical model of the nucleation and growth mechanisms is developed.

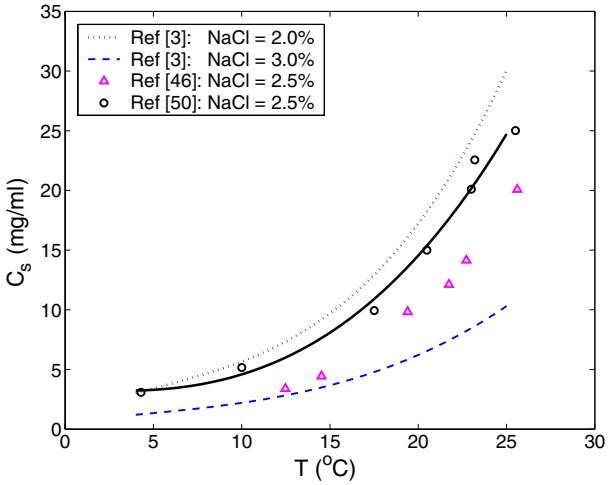

Figure 1. Solubility data of tetragonal lysozyme crystal: dotted and dashed lines show the data in [3], △ show data in [46], ○ show data in [50], and the solid line show the empirical model of equation (1).

2.1. Solubility of the tetragonal HEW lysozyme crystals

The main driving force for the crystal nucleation and growth is understood to be supersaturation, i.e., the concentration of the solution in excess of the saturation concentration (solubility). The solubility of lysozyme at different pH and precipitant concentrations has been studied by [3, 46, 50]. In [3], the solubility experiments covered a pH range from 4.0 to 5.4, NaCl concentration (weight/volume) range from 2.0% to 7.0% and temperature range from 4 to 25 °C. The solubility of HEW lysozyme was also studied in [46], for pH at 4.5, NaCl concentration at 2.1%, 2.5% and 3.0%, and a temperature range from 11 to 30 °C. By implementing a more accurate measurement technique (two-beam interferometry), the solubility in a solution with pH of 4.5 and NaCl concentration of 2.5% was measured in [50].

Since purer samples and more advanced measurement techniques were used in [50], these solubility data, shown as circles in figure 1, are considered to be more accurate and are used to derive parameters of the empirical model in our work. A third-order polynomial is used to fit the data, and the fitted curve is shown as the solid curve in figure 1. Also shown in figure 1 are the solubility data in [3, 46, 50] which exhibit trends similar to the data set obtained in [50], with solubility being low at low temperature and increasing significantly with increasing temperature. The resulting expression for the solubility, $C_s(T)$, is as follows:

$$C_s(T) = 1.0036 \times 10^{-3} T^3 + 1.4059 \times 10^{-2} T^2 - 0.128\,35T + 3.4613. \quad (1)$$

2.2. Modelling of the nucleation rate of the tetragonal HEW lysozyme crystals

For biological molecules, crystals are most often grown with no seeding, where primary nucleation must precede crystal growth. Thus, an understanding of the nucleation process and the effect of various parameters on nucleation is essential for successful production of protein crystals. Recently, significant progress has been made in understanding the nucleation and crystallization of globular proteins, including the formation of compositional and structural crystal defects [48].

Insight into the interactions of protein macro-ions in solution, obtained from light scattering, small-angle x-ray scattering and osmotic pressure studies, shows that the nucleation of globular proteins is governed by the same principles as those of small molecules. In particular, supersaturation, the difference between solute concentration and solubility, is understood to be the main driving force for both nucleation and growth of the protein crystals. Changes of operating conditions, such as lowering temperature, increasing salt concentration, pH or protein concentration, influence nucleation [21] via influencing the solubility. Therefore, to develop an empirical model, it is assumed that the homogenous nucleation rate of the tetragonal HEW lysozyme crystal is only a function of solute concentration and supersaturation. The following two-parameter empirical expression is used as an empirical model to describe the crystal nucleation rate $B(t)$ [17, 2]:

$$B(t) = k_a C \exp\left(-\frac{k_b}{\sigma^2}\right) \quad (2)$$

where σ, the supersaturation, is defined as $\sigma = \ln(C/C_s)$, where C is the solute concentration and C_s is the solubility and k_a and k_b are parameters that are obtained using experimental results.

Different techniques, including light scattering [2], temperature jump [17] and microcalorimetry [9], have been implemented to measure the nucleation rate of the tetragonal HEW lysozyme crystal. We initially use the measurements of concentration and temperature to compute the solubility according to equation (1) and the supersaturation. The experimentally obtained values of the nucleation rate, and the computed concentration and supersaturation values, are then used to obtain the parameters k_a and k_b in equation (2). Both sets of data yield the same values for $k_a = 1044.4\ \text{min}^{-1}\ \text{cm}^{-3}$ and $k_b = 51.33$ and a single straight line serves as the best fit for both sets of data (see figure 2).

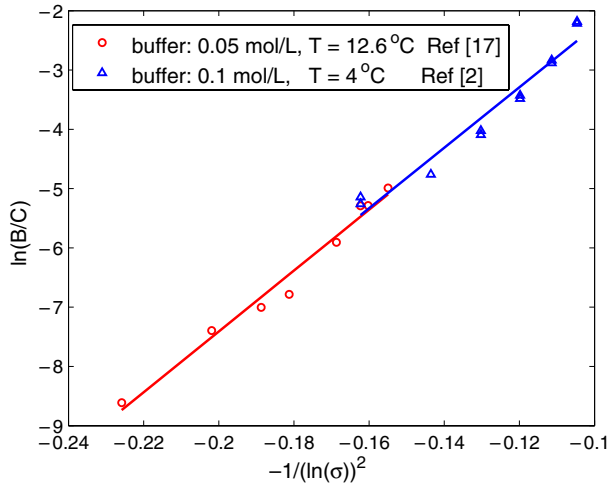

Figure 2. Comparison of the experimental results on the nucleation rate of tetragonal HEW lysozyme crystal: ○ show the data in [17], △ show the data in [2], and the empirical model of equation (2) is shown by the solid line.

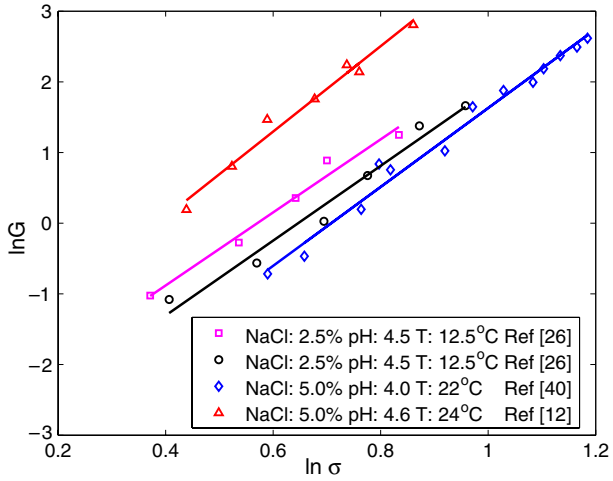

Figure 4. Comparison of the experimental results on the growth rate of tetragonal HEW lysozyme crystal: ◇ show the data in [40], △ show data in [12], and □ and ○ show the data in [26].

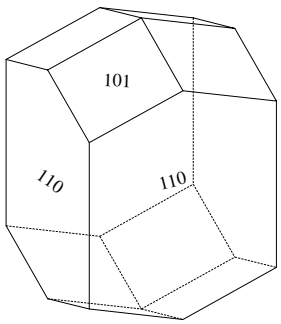

Figure 3. Structure of a tetragonal HEW lysozyme crystal.

2.3. Modelling of the growth rate of tetragonal HEW lysozyme crystals

Figure 3 shows the structure of a tetragonal HEW lysozyme crystal, which shows well-defined facets similar to inorganic crystals. This observation indicates that growth occurs via the spreading of layers from growth step sources such as dislocations and 2D nuclei [11]. The microstructure of the faces of protein crystals has been revealed by implementing advanced measurement techniques, such as electron microscopy and atomic force microscopy (AFM). Experimental results have shown that the growth step generation at screw dislocations outcrops and 2D nucleation islands is the dominant growth mechanism in the growth of tetragonal lysozyme crystals [11]. Experimental studies have also shown that screw dislocations and 2D nucleation are the rate-limiting steps for the growth of tetragonal HEW lysozyme crystals [12, 11, 54]. Detailed spiral growth and 2D nucleation theories have been developed [1]. Experiments in [55] also showed the existence of a critical supersaturation, above which the crystal growth is dominated by 2D nucleation. When the supersaturation is higher than about 1.6, the increase in the growth rate with increasing supersaturation is much faster than at low supersaturation. This is consistent with the results in [12], which concludes that the growth rates at high and low supersaturation are dominated by two different mechanisms. The experimental results suggest that dislocations may be involved in the lysozyme crystal growth at low supersaturation, and 2D nucleation could be dominant at high supersaturation which leads to equal growth rates on all crystal facets, thereby leading to the formation of crystals with morphological regularity. Furthermore, it was found that orthorhombic lysozyme crystals, rather than tetragonal crystals, tend to be formed at low supersaturation [16]. This suggests that the supersaturation should be maintained within appropriate bounds to obtain crystals of desired morphology.

Empirical and theoretical models of crystal growth mechanisms have been developed and compared to experimental results [12, 28, 26]. These works studied the growth rate of the tetragonal HEW lysozyme crystal under various operating conditions, such as different precipitation concentration, solute concentration and temperature. All of them concluded the power-law dependence of the growth rate on supersaturation σ. Some experimental results of the studies of the growth rate of the tetragonal HEW lysozyme crystal are shown in figure 4 [40, 12, 26]. The growth rate data corresponding to the supersaturation are plotted on a log–log scale. It is clear that the growth rate changes exponentially with the supersaturation, and that the value of the exponents obtained from different experiments are very close. In our work, we use the following empirical model to describe the growth rate of the tetragonal HEW lysozyme crystals as a function of supersaturation:

$$G(t) = k_g \sigma^g \tag{3}$$

where k_g is the pre-exponential factor of the growth rate. Since the composition of the solution considered in the present study is the same as that in [26], the experimental data of [26], shown as the circles in figure 4, are used to compute the values of k_g and g in equation (3); this yields $k_g = 3.1451 \times 10^{-9}$ cm min^{-1} and $g = 5.169$.

Table 1. Parameter values for the batch crystallizer model of equations (3) and (4).

k_a	1044.4 ($\text{min}^{-1}\ \text{cm}^{-3}$)	k_g	3.1451×10^{-9} cm min^{-1}
k_b	51.33	g	5.169
k_v	0.54	ρ	1.40×10^3 mg cm^{-3}
U	1800 kJ $\text{m}^{-2}\ \text{h}^{-1}\ \text{K}^{-1}$	A	0.25 m^2
M	10 kg	C_p	4.13 kJ $\text{K}^{-1}\ \text{kg}^{-1}$

3. Modelling of a batch crystallizer for protein crystallization

The mathematical models of particulate processes, including the protein crystallization process in question, are typically obtained through the application of population, material and energy balances and consist of systems of nonlinear partial integro-differential equations that describe the evolution of the particle size distribution (PSD), coupled with systems of nonlinear ordinary differential equations (ODEs) that describe the evolution of the state variables of the continuous phase. There is an extensive literature on population balance modelling, numerical solution, and dynamical analysis of particulate processes; see, for example, [42, 22–24]. See also [8] for further details and references.

For the batch crystallizer considered in this work, a population balance model can be used to describe the evolution of the crystal size distribution (CSD), $n(r, t)$. The evolution of the solute concentration, C, and crystallizer temperature, T, are described by two ODEs. The process model has the following form:

$$\begin{aligned} \frac{\partial n(r,t)}{\partial t} + G(t)\frac{\partial n(r,t)}{\partial r} = 0, \qquad n(0,t) = \frac{B(t)}{G(t)} \\ \frac{\mathrm{d}C}{\mathrm{d}t} = -24\rho k_v G(t)\mu_2(t) \\ \frac{\mathrm{d}T}{\mathrm{d}t} = -\frac{UA}{MC_p}(T - T_\mathrm{j}) \end{aligned} \tag{4}$$

where $G(t)$ is the growth rate, $B(t)$ is the nucleation rate, ρ is the density of crystals, k_v is the volumetric shape factor, U is the overall heat-transfer coefficient, A is the total heat-transfer surface area, M is the mass of solvent in the crystallizer, C_p is the heat capacity of the solution, T_j is the jacket temperature and $\mu_2 = \int_0^\infty r^2 n(r,t)\,\mathrm{d}r$ is the second moment of the CSD. The nucleation rate, $B(t)$, and the growth rate, $G(t)$, are given by equations (2) and (3), respectively, where the parameters obtained from experimental results are used, and reported in table 1. Note that because of the tetragonal form of the crystals and the existence of about 46% of solvent in each crystal [27], the volumetric shape factor, k_v, is set equal to 0.54.

To simulate the population balance model (PBM) of equation (4), a second-order accurate finite difference scheme with sufficient (3000) discretization points is used (while not shown here for the sake of brevity, it was verified that simulations with higher number of discretization points yield results that are almost indistinguishable from those obtained using 3000 discretization points). Figure 5 shows the evolution of the solute concentration (C), the supersaturation (σ) and the CSD at a constant crystallizer temperature ($T = 15\,^\circ$C).

4. Predictive control of the batch protein crystallizer

Early work on control of particulate processes focused mainly on the understanding of fundamental control-theoretic properties of PBMs and the application of conventional control schemes to crystallizers and emulsion polymerization processes; see, e.g., [44], and the references therein. More recently, the realization that PBMs—owing to their infinite-dimensional nature—cannot be used directly for the synthesis of practically implementable model-based controllers, has motivated significant research work on the development of a general order reduction procedure, based on combination of the method of weighted residuals and approximate inertial manifolds, which allows deriving low-order ODE approximations that capture the dominant dynamics of particulate processes and can, therefore, serve as an appropriate basis for the design of low-order controllers that can be readily implemented in practice; see, for example, [6]. This approach subsequently laid the foundation for the development of a systematic framework for solving a number of important control problems for particulate processes, including the problem of dealing with the highly nonlinear behaviour, for example, owing to complex growth, nucleation, agglomeration and breakage mechanisms, and the Arrhenius dependence of nucleation laws on solute concentration in crystallizers [6], the problem of control under model uncertainty [7], and the problem of control under actuator constraints [13].

The crystal size distribution or the moments of the crystal size distribution are often not available as online measurements. Solute concentration and temperature, on the other hand, are more readily available as measurements and can be used to generate estimates of the moments which are required for implementation of feedback control strategies based on the reduced-order moments model. Also, given the availability of a reduced-order moments model and estimates of the moments, desirable product characteristics need to be appropriately expressed in terms of constraints on the crystal size distribution, and physical limitations on the manipulated variable (jacket temperature) must be accounted for in the control design. In this work we focus on developing a control strategy that is applicable to several crystallization processes, and not on demonstrating it on a specific experimental setup. Such an experimental implementation is outside the scope of this work; yet practical issues such as fast computation of control action, testing for robustness, availability of software for implementation, and availability of measurements are accounted for. To this end, in the remainder of this section we first use model reduction techniques to develop a reduced-order model suitable for the purpose of real-time control. Next, we present the design of a state estimator, to provide estimates of the states of the reduced-order model using available measurements. Then we present a predictive controller design that uses the state estimates for the purpose of real-time control, while incorporating performance considerations as appropriate constraints on the moments of the crystal size distribution and accounting for the constraints on the manipulated input variable.

4.1. Model reduction

Owning to the fact that the dominant dynamics of the crystallizer are characterized by a small number of degrees of

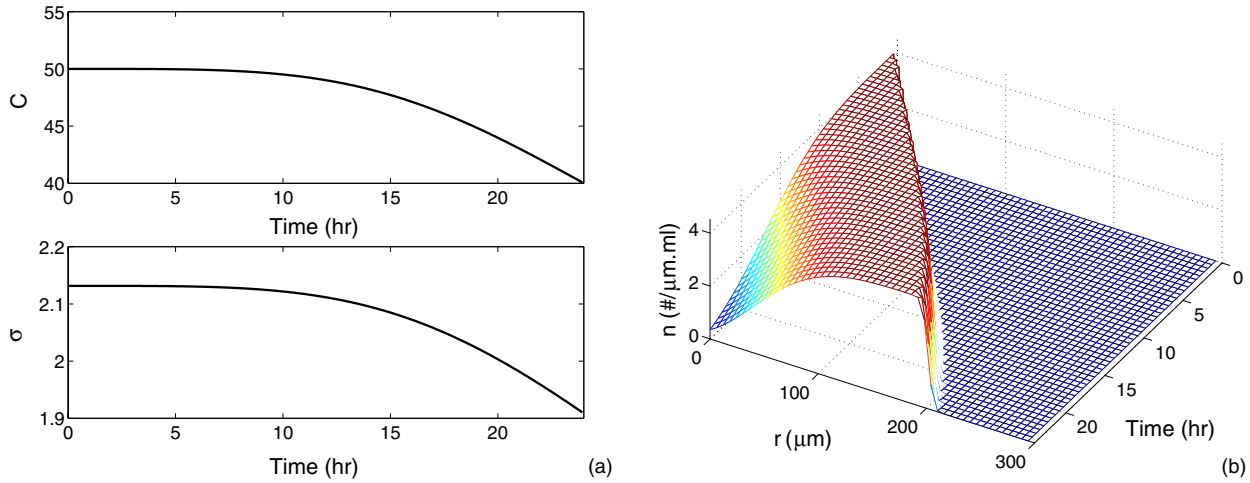

Figure 5. Open-loop simulation results of the solute concentration (C), the supersaturation (σ) and the CSD at a constant crystallizer temperature ($T = 15\,^{\circ}\mathrm{C}$).

freedom [6], the method of moments [19] (see also [8, 52, 30]) is applied to the system of equation (4) to derive an approximate ODE model. Defining the ith moment of $n(r, t)$ as

$$\mu_i = \int_0^\infty r^i n(r,t)\,\mathrm{d}r, \qquad i = 0, 1, \ldots, \infty, \tag{5}$$

multiplying the population balance in equation (4) by r^i, and integrating over all crystal sizes, the following infinite set of ordinary differential equations, which describes the rate of change of the moments of the crystal size distribution, solute concentration and temperature, is obtained:

$$\begin{aligned}
\frac{\mathrm{d}\mu_0}{\mathrm{d}t} &= B(t)\\
\frac{\mathrm{d}\mu_i}{\mathrm{d}t} &= \mathrm{i}G(t)\mu_{i-1}(t), \qquad i = 1, 2, \ldots, \infty\\
\frac{\mathrm{d}C}{\mathrm{d}t} &= -24\rho k_v G(t)\mu_2(t)\\
\frac{\mathrm{d}T}{\mathrm{d}t} &= -\frac{UA}{MC_p}(T - T_\mathrm{j}).
\end{aligned} \tag{6}$$

Note that in equations (6), the ODEs describing the dynamics of the first N moments, where N is any positive integer greater than or equal to 3, the solute concentration and the crystallizer temperature are independent of the moments of order $N+1$ and higher. This implies that a set of ODEs, which include the first N moments and the evolution of the solute concentration and crystallizer temperature, would provide an accurate description of the evolution of the first N moments, the solute concentration and the crystallizer temperature. In this case, the nucleation and growth rates are independent of crystal size, and this allows closure of the moment equations (note that closure can still be achieved if the nucleation and growth mechanism are dependent on certain moments of the crystal size distribution). In cases where the moments do not close, a finite set of ODEs describing the evolution of the moments would provide an approximation that gets increasingly accurate as the number of moments included in the reduced-order model is increased.

As will be seen in section 4.3, the control objective will require computation of μ_3 and μ_4, hence N is chosen as 4 and the following reduced-order model is used for the purpose of controller design:

$$\begin{aligned}
\frac{\mathrm{d}\mu_0}{\mathrm{d}t} &= B(t)\\
\frac{\mathrm{d}\mu_i}{\mathrm{d}t} &= \mathrm{i}G(t)\mu_{i-1}(t), \qquad i = 1, 2, 3, 4\\
\frac{\mathrm{d}C}{\mathrm{d}t} &= -24\rho k_v G(t)\mu_2(t)\\
\frac{\mathrm{d}T}{\mathrm{d}t} &= -\frac{UA}{MC_p}(T - T_\mathrm{j}).
\end{aligned} \tag{7}$$

4.2. State estimator design

In this section, we present an observer design that uses measurements of the solute concentration, C, and temperature T and the reduced-order moments model, to generate estimates of the moments. Note that building an observer for a nonlinear system of the form of equation (7) with guaranteed convergence properties is in general a difficult task. In this work, an extended Luenberger-type observer is used to estimate the values of the moments of the CSD and takes the following form:

$$\begin{aligned}
\frac{\mathrm{d}\hat{\mu}_0}{\mathrm{d}t} &= \hat{B}(t) + L_0(C_m - \hat{C})\\
\frac{\mathrm{d}\hat{\mu}_i}{\mathrm{d}t} &= \mathrm{i}\hat{G}(t)\hat{\mu}_{i-1}(t) + L_i(C_m - \hat{C}), \qquad i = 1, \ldots, 4\\
\frac{\mathrm{d}\hat{C}}{\mathrm{d}t} &= -24\rho k_v \hat{G}(t)\hat{\mu}_2(t) + L_5(C_m - \hat{C})
\end{aligned} \tag{8}$$

where C_m is the online measurement of the solute concentration, $\hat{B}(t)$ and $\hat{G}(t)$ are the nucleation and growth rates computed using the online measurement of T and values of the estimates of $\hat{\mu}_i$ and $\hat{C}$, and L_i, $i = 0, \ldots, 5$ are the observer gains (these values were obtained via running open-

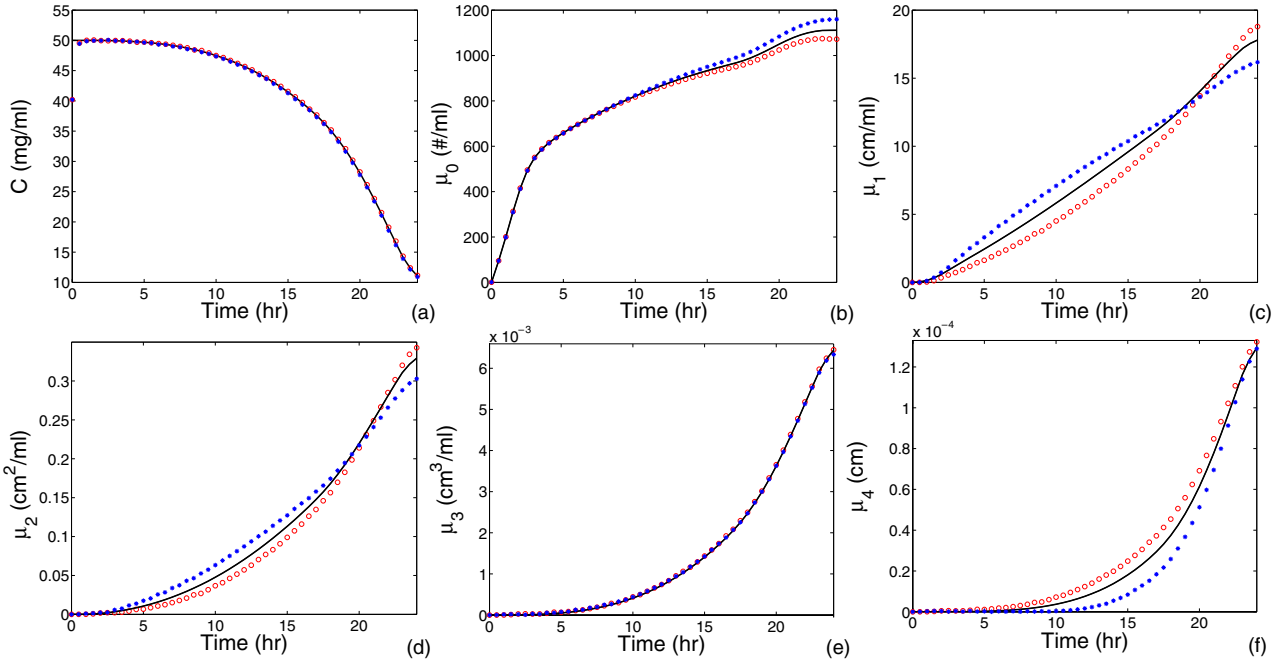

Figure 6. Comparison between the true value and the estimates of C (the solute concentration) and μ_i, $i = 0, 1, \ldots, 4$.

Table 2. Parameter values for the Luenberger-type observer of equation (8).

L_0	-0.4	L_1	0.05
L_2	0.001	L_3	1.7×10^{-5}
L_4	3×10^{-7}	L_5	-0.1

loop simulations and comparing the evolution of the state with the state estimates for different choices of stabilizing observer gains), reported in table 2.

Figures 6(a)–(f) show a comparison between the evolution of the solute concentration (solid line in figure 6(a)) and the moments $\mu_i, i = 0, 1, \ldots, 4$ (solid lines in figures 6(b)–(f)) and the estimates of the solute concentration C and the moments, for the perfect model case (dotted lines), and for two instances of plant-model mismatch, where the parameter g in the moment model is 90% and 110% of its nominal value, respectively (denoted by ○ and $*$), under open-loop simulations. In all instances, the effect of measurement noise, often found in experimental readings, is simulated by introducing a white noise with variance of 0.5 mg ml^{-1} in the measurement of the solute concentration. Furthermore, to evaluate the convergence of the estimates to the true state values, the initial value of the estimated solute concentration, $\hat{C}$, is set to 40 mg ml^{-1}, while the true value is 50 mg ml^{-1}.

Note that for the batch crystallization considered in this work, the initial values of the moments at the beginning of the batch run are identically equal to zero, because there are no crystals initially inside the crystallizer. In the case of a perfect model, the state estimates converge quickly to the true values, and in both cases of plant-model mismatch, the observer generates satisfactory estimates of the states (see figures 6(a)–(f)).

4.3. Predictive controller formulation

Significant previous work has focused on CSD control in batch crystallizers, e.g., [43, 58]. In [36], an open-loop optimal control strategy was derived, where the objective function involves maximization of the crystal size, and the cooling curve is the decision variable. In [34], a method was developed for assessing parameter uncertainty and studying its effects on the open-loop optimal control strategy, which maximized the weight mean size of the product. An online optimal control methodology was developed for a seeded batch cooling crystallizer in [58, 59]. Most of these works focused on open-loop optimal control of the batch crystallizer, i.e., the optimal operating condition is calculated off-line and implemented during the batch operation. The successful achievement of the control objective in such a control strategy depends heavily on the accuracy of the models, and disturbances affecting the batch operation may easily drive the process off the desired trajectory. The volume-averaged crystal size is an important parameter that characterizes the crystal size distribution [59], especially for pharmaceuticals. A larger volume-averaged crystal size facilitates downstream processing of the crystals, such as filtration. As mentioned previously, experimental results show that low supersaturation leads to the cessation of the crystal growth, while needle-like, instead of tetragonal crystals, form if the supersaturation is too high, and this necessitates maintaining the supersaturation (and similarly, temperature) within an acceptable range. Constraints on the jacket temperature reflect the physical limitations in supplying the coolant at a prescribed temperature.

In the case of continuous operation of the crystallizers, the overriding objective is often stabilization, and the presence of constraints on the manipulated input variables limits the set of initial conditions starting from where stabilization can be achieved (this also motivates using predictive controllers in

a way that allows for computing explicitly the set of initial conditions starting from where stabilization can be achieved; see, for example [15, 32, 33], for hybrid predictive control designs for linear systems under state and output feedback control, and for nonlinear systems subject to uncertainty, respectively, and [14] for an application of the hybrid predictive controllers to a continuous crystallization process example). For batch processes, in contrast, the expression of performance considerations in the form of appropriate constraints or in the objective function, and achieving a desired product size distribution, are more important issues. Based on these considerations, we present in the remainder of this section a predictive controller formulation where, at time t_i, the control trajectory is computed by solving an optimization problem of the form

$$\begin{aligned}
&\min -\frac{\mu_4(t_f)}{\mu_3(t_f)}\\
&\text{s.t. } \frac{\mathrm{d}\mu_0}{\mathrm{d}t} = k_a C \exp\left(-\frac{k_b}{\sigma^2}\right)\\
&\frac{\mathrm{d}\mu_i}{\mathrm{d}t} = \mathrm{i}k_g \sigma^g \mu_{i-1}(t), \qquad i = 1, \ldots, 4\\
&\frac{\mathrm{d}C}{\mathrm{d}t} = -24\rho k_v k_g \sigma^g \mu_2(t)\\
&\frac{\mathrm{d}T}{\mathrm{d}t} = -\frac{UA}{MC_p}(T - T_\mathrm{j})
\end{aligned} \tag{9}$$

$$\begin{aligned}
&\mu_i(t_i) = \hat{\mu}_i(t_i) \qquad C(t_i) = \hat{C}(t_i)\\
&t_i \leqslant t \leqslant t_f \qquad T_{\min} \leqslant T \leqslant T_{\max}\\
&T_{\mathrm{j}\min} \leqslant T_\mathrm{j} \leqslant T_{\mathrm{j}\max} \qquad \sigma_{\min} \leqslant \sigma \leqslant \sigma_{\max},\\
&\left|\frac{\mathrm{d}C_\mathrm{s}}{\mathrm{d}t}\right| \leqslant k_1
\end{aligned}$$

$$n(0, t) \leqslant n_{\mathrm{fine}}, \qquad \forall t \geqslant t_f/2 \tag{10}$$

where $T_{\min}$ and $T_{\max}$ are the constraints on the crystallizer temperature, T, and are specified as 4 and 22 °C, respectively. $T_{\mathrm{j}\min}$ and $T_{\mathrm{j}\max}$ are the constraints on the manipulated variable, T_j, and are specified as 3 and 22 °C, respectively. The constraints on the supersaturation σ are $\sigma_{\min} = 1.73$ and $\sigma_{\max} = 2.89$. The constant, k_1 (chosen to be 0.065 mg ml^{-1} min^{-1}), specifies the maximum rate of change of the saturation concentration C_s. n_{fine} is the largest allowable number of nuclei at any time instant during the second half of the batch run, and is set to be 5 μm^{-1} ml^{-1}. Previous work has shown that the objective of maximizing the volume-averaged crystal size can result in a large number of fines in the final product [29]. The constraint of equation (10), by restricting the number of nuclei formed at any time instant during the second half of the batch run, limits the fines in the final product.

In the closed-loop control structure, the PBM, together with the mass and energy balances of equation (4), is used to simulate the batch crystallization process. Measurements of the solute concentration and the crystallizer temperature are assumed to be available, and are used by the Luenberger-type observer of equation (8) to generate estimates of the moments. These estimates are used as initial conditions of the states in the moments model, which is used in the predictive controller to compute the control trajectory. Specifically, the PBM is utilized to simulate the value of the state variables (n, C, T) at $t_i = \mathrm{i}\Delta t$, where $i = 1, 2, \ldots, m$, $m = t_f/\Delta t$, and t_f is the length of the crystallization period. The measurements of C and T are used to compute estimates of $\hat{\mu}_\mathrm{j}(t_i)$. These estimates are used as initial values of the states in the reduced-order moments model, and used within the optimization problem over a horizon length of $t_f - t_i$ to compute the optimal control trajectory. The first step of the solution (T_j) is implemented in the closed loop, and this procedure is repeated every Δt until the end of the batch run. In the simulations, Δt and t_f are chosen as 5 min and 24 h, respectively. Equation (4), which describes the evolution of the batch crystallizer, is solved by a second-order accurate finite difference scheme with 3000 spatial discretization points and 7200 temporal discretization points, and the optimization problem is solved using sequential quadratic programming (SQP).

5. Closed-loop simulation results

We first demonstrate the effect of the unavailability of measurements of the moments on the evolution of the closed-loop system. To this end, we compare the following scenarios:

(1) state feedback control (i.e., the measurements of the moments are available); the control trajectory initially computed by the optimization problem is shown by the dotted line, and the closed-loop control trajectory under state feedback is shown by the dash–dotted line in figure 7(a), and
(2) output feedback control; the control trajectory initially computed by the optimization problem is shown by the dashed line in figure 7(a), and the closed-loop control trajectory under output feedback control is shown by the solid line in figure 7(a) (the corresponding supersaturation profiles are shown in figure 7(b)).

Note that in the case of state feedback control, the control trajectory computed initially coincides with that under the closed-loop implementation (the dotted and dash–dotted lines overlap), since the tail of the control trajectory continues to be the solution to the optimization problem at the successive times. In the case of output feedback control, however, the control trajectory is initially computed based on the available (incorrect) estimates of the state variables, and leads to state constraints violation if implemented for the entire duration of the batch run (see dashed lines in figure 7(b), where the supersaturation hits the lower constraint at $t = 18.2$ h).

Next, we compare the performance of the proposed predictive controller to that of three other control strategies, constant temperature control (CTC), constant supersaturation control (CSC) and open-loop optimal control strategy. To study the ability of the proposed predictive control strategy to maximize the performance objective while avoiding the formation of a large number of fines in the final product, the predictive controller of equation (9) is implemented with the additional constraint (equation (10)) on the fines in the final product. Also, to evaluate the robustness of the proposed method with respect to plant-model mismatch, we consider a 10% error in the nominal value of the parameter g—which

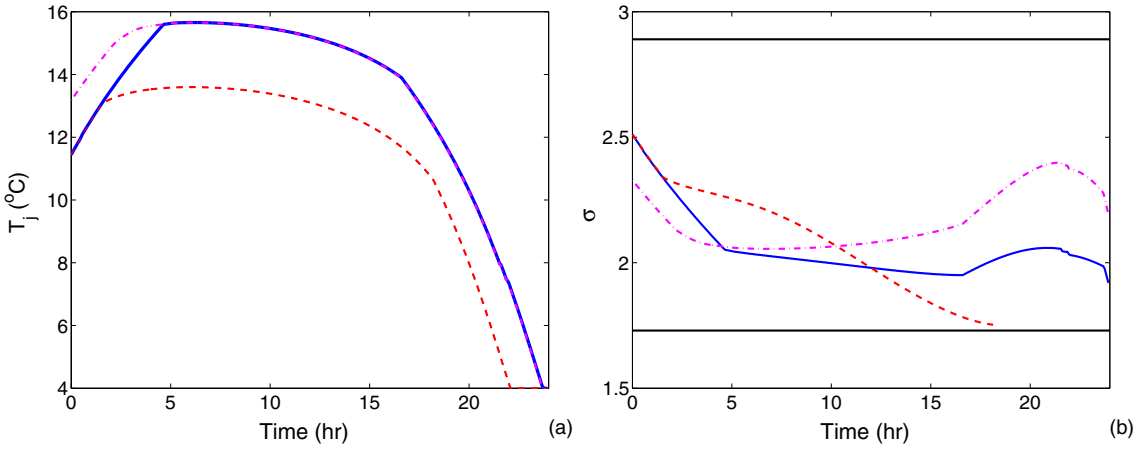

Figure 7. (a) Jacket temperature and (b) supersaturation profiles under (1) state feedback control: dotted (implementation of the initially computed manipulated input trajectory) and dash–dotted (closed-loop state feedback control) lines, and (2) output feedback control; dashed (implementation of the initially computed manipulated input trajectory) and solid (closed-loop output feedback control) lines.

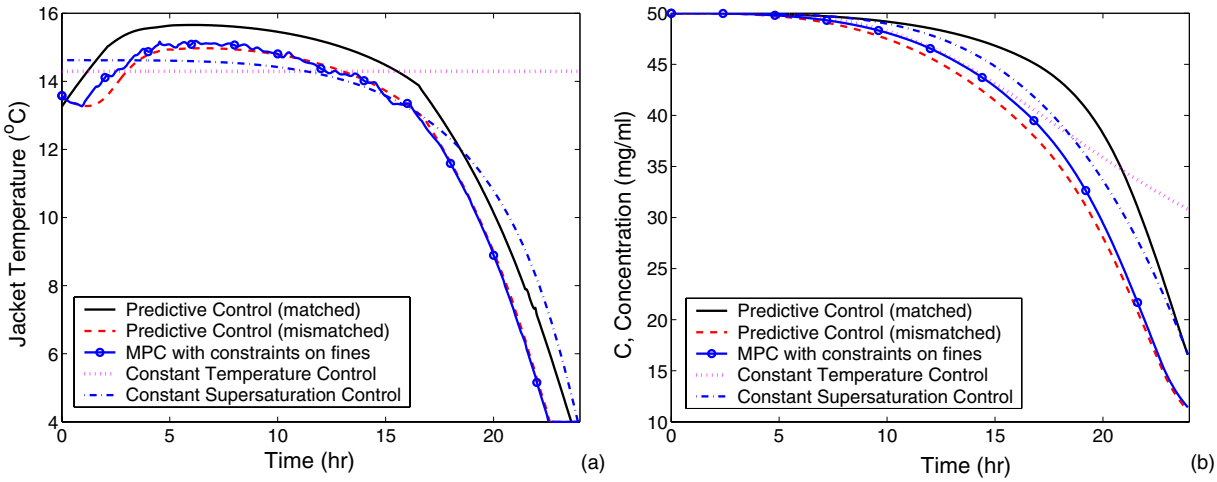

Figure 8. Comparison of the simulation results for (a) jacket temperature and (b) solute concentration under four different control strategies.

is the exponent relating growth rate to supersaturation—in the moments model used in the predictive controller.

In figures 8 and 9, four important variables, the jacket temperature, the solute concentration, the supersaturation, and the volume distribution of the CSD ($P(r)$) at the end of the batch run, are shown. The volume distribution of the CSD, $P(r)$, defined as

$$P(r) = \frac{r^3 n(r, t_f)}{\int_0^\infty r^3 n(r, t_f)\, \mathrm{d}r} \tag{11}$$

where t_f is the time at the end of the batch run, is an important variable in determining the product characteristics. The two horizontal lines at 1.73 and 2.89 in figure 9(a) are the lower and upper constraints on the supersaturation. The evolution of the CSD under different control strategies is shown in figure 10.

Figure 8(a) shows the comparison of the manipulated variable trajectories, the jacket temperature T_j, for the five scenarios. Note that while the trajectories of the jacket temperature under CSC (dash–dotted line) and under the predictive controller with a matched model (solid line) are close, the slight difference causes the behaviour of the CSD evolution under these two different control strategies to be significantly different (shown in figures 10(a) and (e)), indicating the necessity to implement control to achieve a desired product quality.

Since the supersaturation σ is the main driving force for the crystal nucleation and growth, the evolution of supersaturation under various control strategies, shown in figure 9(a), can be subsequently used to explain the behaviour of the CSD evolution. Specifically, the solid line in figure 9(a) shows that the predictive controller computes a manipulated input trajectory that results in the supersaturation first decreasing, then staying almost constant at a low level, and finally increasing at the end of the batch run. In view of the fact that the control objective is to maximize the volume-averaged crystal size at the end of the batch run, i.e., to maximize the volume of big crystals while minimizing the volume of small crystals, the result can be understood as follows: after high initial levels of supersaturation, which results in a number of nuclei being formed, a drop in the supersaturation results in the nucleation rate dropping more drastically than the growth

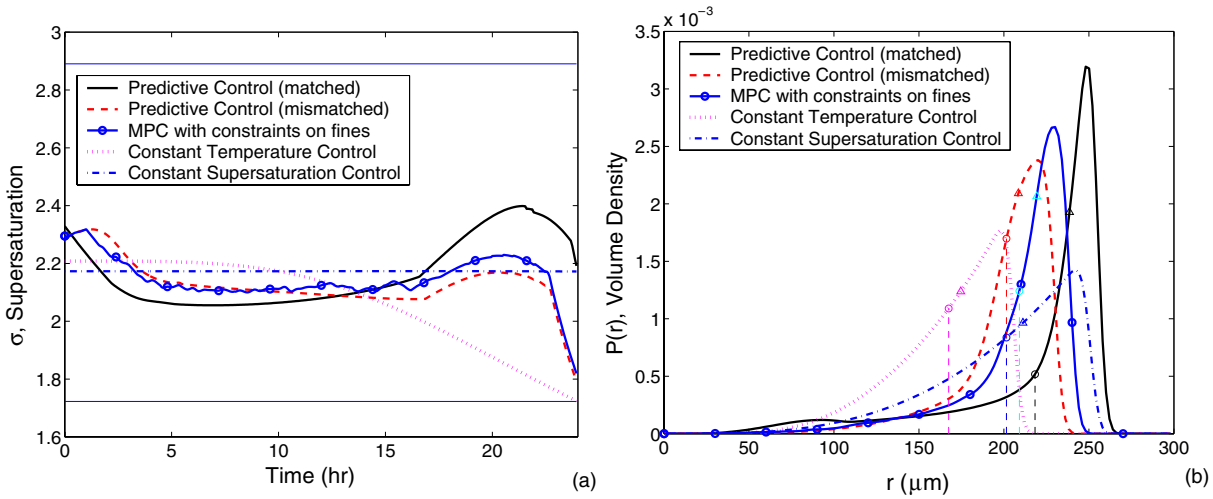

Figure 9. Comparison of the simulation results for (a) supersaturation and (b) volume density under four different control strategies.

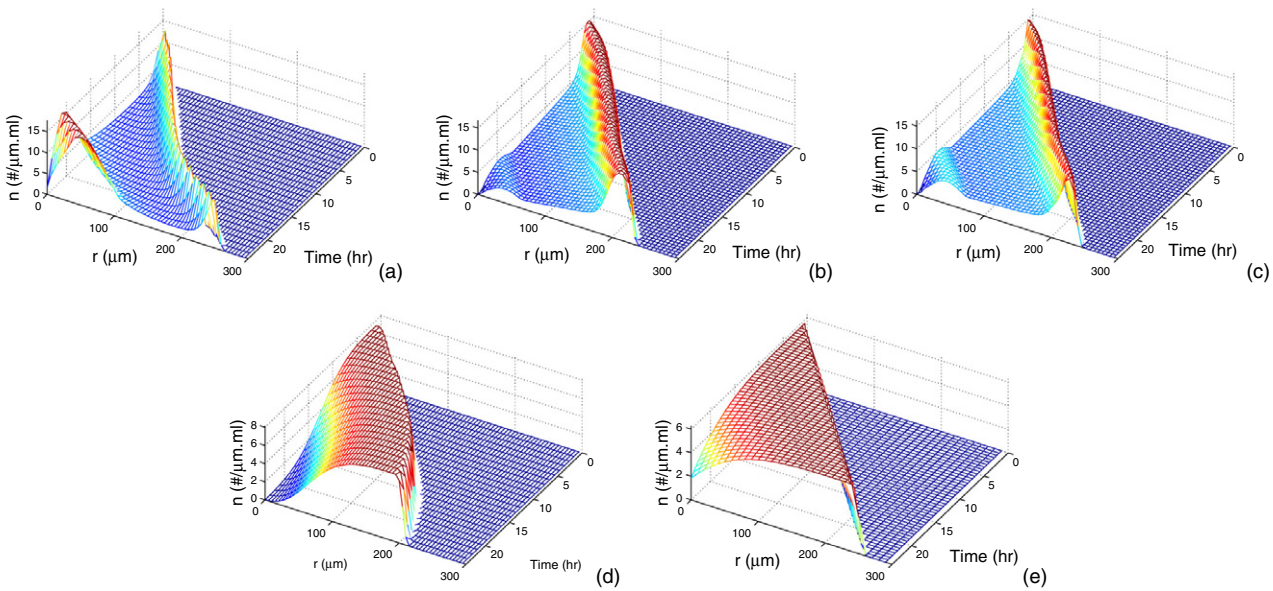

Figure 10. Evolution of crystal size distribution under four different control strategies: (a) predictive control with matched model, (b) predictive control with mismatched model, (c) predictive control with constraint on fines, (d) constant temperature control, (e) constant supersaturation control.

rate (note that while the nucleation rate in equation (2) shows exponential dependence on the supersaturation, the growth rate in equation (3) exhibits a power-law dependence), and favours growth of the initially formed crystals instead of the formation of new crystals. Towards the end of the batch run, it is advantageous to increase the growth rate (by increasing the supersaturation) to maximize the size of the crystals in the batch reactor, even at the cost of forming a small number of new nuclei because the net result is a favourable increase in the volume-averaged crystal size.

Note that, towards the end of the batch run, the solute concentration has depleted due to the formation of crystals. Supersaturation, however, is the solute concentration in excess of the solubility, and it may be increased by decreasing the solubility, which is a function of the reactor temperature. Therefore, the desired increase in the supersaturation at the end of the batch run is achieved by lowering the jacket temperature (to lower the reactor temperature, which lowers the solubility, and hence increases the supersaturation), until it hits the lower constraint (4 °C) on the jacket temperature. Together with reinforcing the notion that a timely drop in the supersaturation during crystal growth can consistently produce larger crystals, the proposed method provides a framework for deciding both the time and amount of decrease in supersaturation (due to the optimality properties of the proposed method) and also accounting for process-model mismatch via feedback (because of using an online control strategy). In other words, this work does not provide a recipe (which naturally springs forth the question of applicability to other proteins) but provides a framework for computing the 'optimal' control strategy for the

Table 3. Comparison between the simulation results under five different control strategies.

Control strategy	μ_4/μ_3 (μm)	μ_3 ($\times 10^3$)	r_{10} (μm)	r_{50} (μm)	r_{90} (μm)	Span
Predictive control (matched)	218	5.589	143	239	253	0.463
Predictive control (mismatched)	201	6.459	167	208	226	0.284
Predictive control with constraint on fines	208	6.374	166	219	235	0.315
Open-loop CTC	168	3.186	123	175	201	0.445
Open-loop CSC	201	5.583	143	211	244	0.478

specific protein crystallizer under consideration. For different proteins, the optimal control trajectories could be different because of the different nucleation and growth mechanism, but this would naturally result from the implementation of the proposed method to the protein under consideration.

The closed-loop simulation results for the case of a process-model mismatch are shown by the dashed line in figures 8, 9 and 10(b). Comparing figures 10(a) and (b), it is clear that through feedback, the predictive controller 'corrects' for plant-model mismatch and produces a different manipulated input trajectory to enforce constraint satisfaction and achieve the desired objective. Simulation results, shown in figure 7, also demonstrate that if the off-line optimized trajectory of jacket temperature, based on the mismatched model, is implemented for the entire duration of the batch run without using the measurements to update the control trajectory, the state constraints are violated at the end of the batch run. This observation underscores the fact that, while the proposed approach provides valuable improvements in the objective (that of maximizing the volume averaged crystal size), the ability to enforce constraints is perhaps more valuable in experimental setups, where the process-model mismatch necessitates feedback (as opposed to the implementation of open-loop optimal control strategies, such as CSC or CTC) to ensure that the constraints are satisfied during the entire batch run.

Note that predictive control without constraint on fines can result in a product with a large number of fines (see figure 10(a)), which is undesirable. The implementation of the predictive controller with the constraint of equation (10), designed to reduce the fines in the product, results in a product with much fewer fines while still maximizing the volume-averaged crystal size (see figure 10(c) and table 3).

Compared to predictive control, the crystal size distribution evolves very differently under CTC and CSC. Under CTC, where a constant reactor temperature is maintained throughout the batch run, the control strategy results in a constant solubility during the batch run, and the depletion in the solute concentration is reflected in the decrease of supersaturation, which eventually hits its lower constraint (the dotted line in figure 9(a)). In contrast, under CSC, which tries to maintain a constant value of the supersaturation during the entire batch run, the reactor temperature is lowered during the entire batch run (via the continued lowering of the jacket temperature) to keep up with the falling concentration levels (see the dash–dotted line in figures 8(a) and 9(a)). Under CSC, therefore, the growth rate stays constant during the batch run, since it is only dependent on the supersaturation. The nucleation rate, which also depends directly on the solute concentration itself, is lowered gradually because of the depletion of the solute. Unlike the CSD evolution under predictive control, in the case of CTC and CSC, a constant number of new nuclei are continuously formed during the whole batch run until the depletion of the solute, and this leads to a relatively low volume-averaged crystal size compared to the case of crystallizer operation under predictive control.

Table 3 summarizes the simulation results obtained under the five different control strategies:

(1) Predictive control with a matched model.
(2) Predictive control with a mismatched model.
(3) Predictive control with constraint on fines.
(4) Open-loop operation under CTC, and
(5) Open-loop operation under CSC.

In table 3, six characteristic parameters of the product at the end of the batch run are compared, including the value of the volume-averaged crystal size (μ_4/μ_3), total volume (μ_3), r_{10}, r_{50}, r_{90} and the span. r_{10}, r_{50} and r_{90} are the 10%, 50% and 90% volume fractions of the CSD, respectively, denoting the percentage of crystals smaller than that size. The span, defined as $(r_{90} - r_{10})/r_{50}$, is an important characteristic of the CSD, and is widely used in the pharmaceutical industry. A high span value indicates a wide distribution in size and a high polydispersity, which is undesirable.

Comparing the results of the five control strategies listed in table 3, it is clear that the predictive controller increases the volume-averaged crystal size by 30% compared to CTC, and 8.5% compared to CSC. It is also observed that, in the case of process-model mismatch (a 10% error of the exponent relating growth rate to supersaturation), the predictive control strategy is able to increase the volume-averaged crystal size by 20% compared to CTC. Although the predictive controller with a mismatched model results in a similar volume-averaged crystal size compared to CSC, it leads to a much higher volume of the product, 103% compared to CTC and 16% compared to CSC. Note also that the CSD under predictive control has the largest r_{10}, r_{50} and r_{90}. Figure 9(b) shows that the CSDs under the proposed predictive controller with perfect model (solid line), plant-model mismatch (dashed line) and constraint on fines (solid line marked with circles) have lower polydispersity. A lower span and much larger volume-averaged crystal size are achieved under predictive control with constraint on fines compared to the one under CTC and CSC, as shown in figure 10 and table 3. In summary, the implementation of the proposed predictive controller increases the volume-averaged crystal size, satisfies state and input constraints, and is found to be robust with respect to plant-model mismatch.

6. Conclusions

In this work, we considered the problem of modelling, simulation and control of a batch protein crystallization process that is used to produce the tetragonal HEW lysozyme crystals. First, a population balance model, using empirically obtained rate expressions, was developed to simulate the batch crystallization process. Then, model reduction techniques were used to derive a reduced-order moments model for the purpose of controller design. Online measurements of the solute concentration and reactor temperature were assumed to be available, and a Luenberger-type observer was used to estimate the moments of the crystal size. A predictive controller, which uses these state estimates, was designed to achieve the objective of maximizing the volume-averaged crystal size while respecting constraints on the manipulated input variables (which reflect physical limitations of control actuators) and on the process state variables (which reflect performance considerations). Simulation results showed that the proposed predictive controller was able to increase the volume-averaged crystal size by 30% and 8.5% compared to constant temperature control (CTC) and constant supersaturation control (CSC) strategies, respectively, while reducing the number of fine crystals produced. Furthermore, a comparison of the crystal size distributions (CSDs) indicated that the product achieved by the proposed predictive control strategy has larger total volume and lower polydispersity compared to the CTC and CSC strategies. Finally, the robustness of the proposed method with respect to plant-model mismatch was evaluated. In contrast to open-loop control strategies, which led to violation of constraints in the presence of plant-model mismatch, the proposed method was demonstrated to successfully achieve the task of maximizing the volume-averaged crystal size while satisfying the state and input constraints.

Acknowledgment

Financial support from NSF, CTS-0129571, is gratefully acknowledged.

References

[1] Bennema P 1984 Spiral growth and surface roughening: developments since Burton, Cabrera and Frank *J. Cryst. Growth* **69** 182–97

[2] Bhamidi V, Varanasi S and Schall C A 2002 Measurement and modeling of protein crystal nucleation kinetics *Cryst. Growth Design* **2** 395–400

[3] Cacioppo E and Pusey M L 1991 The solubility of the tetragonal form of hen egg white lysozyme from pH 4.0 to 5.4 *J. Cryst. Growth* **114** 286–92

[4] Carter D C *et al* 1999 Lower dimer impurity incorporation may result in higher perfection of HEWL crystals grown in microgravity: a case study *J. Cryst. Growth* **196** 623–37

[5] Chayen N E and Saridakis E 2001 Is lysozyme really the ideal model protein? *J. Cryst. Growth* **232** 262–4

[6] Chiu T and Christofides P D 1999 Nonlinear control of particulate processes *AIChE J.* **45** 1279–97

[7] Chiu T and Christofides P D 2000 Robust control of particulate processes using uncertain population balances *AIChE J.* **46** 266–80

[8] Christofides P D 2002 *Model-Based Control of Particulate Processes* (Dordrecht: Kluwer–Academic)

[9] Darcy P A and Wiencek J M 1999 Identifying nucleation temperatures for lysozyme via differential scanning calorimetry *J. Cryst. Growth* **196** 243–9

[10] DeMattei R C and Feigelson R S 1992 Controlling nucleation in protein solutions *J. Cryst. Growth* **122** 21–30

[11] Durbin S D, Carlson W E and Saros M T 1993 *In situ* studies of protein crystal-growth by atomic-force microscopy *J. Phys. D: Appl. Phys.* **26** B128–32

[12] Durbin S D and Feher G 1986 Crystal growth studies of lysozyme as a model for protein crystallization *J. Cryst. Growth* **76** 583–92

[13] El-Farra N H, Chiu T and Christofides P D 2001 Analysis and control of particulate processes with input constraints *AIChE J.* **47** 1849–65

[14] El-Farra N H, Mhaskar P and Christofides P D 2004 Hybrid predictive control of nonlinear systems: method and applications to chemical processes *Int. J. Robust and Nonlinear Control* **4** 199–225

[15] El-Farra N H, Mhaskar P and Christofides P D 2004 Uniting bounded control and MPC for stabilization of constrained linear systems *Automatica* **40** 101–10

[16] Forsythe E L, Nadarajah A and Pusey M L 1999 Growth of (101) faces of tetragonal lysozyme crystals: measured growth-rate trends *Acta Crystallogr.* D **55** 1005–11

[17] Galkin O and Vekilov P G 1999 Direct determination of the nucleation rates of protein crystals *J. Phys. Chem.* B **103** 10965–71

[18] Hu S Y B, Wiencek J M and Arnold M A 2001 Application of near-infrared spectra on temperature-controlled protein crystallization—a simulation study *Appl. Biochem. Biotechnol.* **94** 179–96

[19] Hulburt H M and Katz S 1964 Some problems in particle technology: a statistical mechanical formulation *Chem. Eng. Sci.* **19** 555–74

[20] Jones W F, Arnold M A and Wiencek J M 2004 Precipitant-controlled growth of lysozyme crystals in sodium thiocyanate *Cryst. Growth Design* **4** 1387–93

[21] Judge R A, Jacobs R S, Frazier T, Snell E H and Pusey M L 1999 The effect of temperature and solution pH on the nucleation of tetragonal lysozyme crystals *Biophys. J.* **77** 1585–93

[22] Kalani A and Christofides P D 1999 Nonlinear control of spatially-inhomogeneous aerosol processes *Chem. Eng. Sci.* **54** 2669–78

[23] Kalani A and Christofides P D 2000 Modeling and control of a titania aerosol reactor *Aerosol. Sci. and Technol.* **32** 369–91

[24] Kalani A and Christofides P D 2002 Simulation, estimation and control of size distribution in aerosol processes with simultaneous reaction, nucleation, condensation and coagulation *Comput. Chem. Eng.* **26** 1153–69

[25] Kierzek A M and Zielenkiewicz P 2001 Models of protein crystal growth *Biophys. Chem.* **91** 1–20

[26] Kurihara K, Miyashita S, Sazaki G, Nakada T, Suzuki Y and Komatsu H 1996 Interferometric study on the crystal growth of tetragonal lysozyme crystal *J. Cryst. Growth* **166** 904–8

[27] Leung A K W, Park M M V and Borhani D W 1999 An improved method for protein crystal density measurements *J. Appl. Crystallogr.* **32** 1006–9

[28] Li M, Nadarajah A and Pusey M L 1995 Modeling the growth rates of tetragonal lysozyme crystals *J. Cryst. Growth* **156** 121–32

[29] Ma D L, Tafti D K and Braatz R D 2002 Optimal control and simulation of multidimensional crystallization processes *Comput. Chem. Eng.* **26** 1103–16

[30] Mantzaris N V and Daoutidis P 2004 Cell population balance modeling and control in continuous bioreactors *J. Process Control* **14** 775–84

[31] McPherson A 1991 A brief history of protein crystal growth *J. Cryst. Growth* **110** 1–10

[32] Mhaskar P, El-Farra N H and Christofides P D 2004 Hybrid predictive control of process systems *AIChE J.* **50** 1242–59
[33] Mhaskar P, El-Farra N H and Christofides P D 2005 Robust hybrid predictive control of nonlinear systems *Automatica* **41** 209–17
[34] Miller S M and Rawlings J B 1994 Model identification and control strategies for batch cooling crystallizers *AIChE J.* **40** 1312–27
[35] Monaco L A and Rosenberger F 1993 Growth and etching kinetics of tetragonal lysozyme *J. Cryst. Growth* **129** 465–84
[36] Mullin J W and Nyvlt J 1971 Programmed cooling of batch crystallizers *Chem. Eng. Sci.* **26** 369–77
[37] Nagatoshi Y, Sazaki G, Suzuki Y, Miyashita S, Matsui T, Ujihara T, Fujiwara K, Usami N and Nakajima K 2003 Effects of high pressure on the growth kinetics of orthorhombic lysozyme crystals *J. Cryst. Growth* **254** 188–95
[38] Przybylska M 1989 A double cell for controlling nucleation and growth of protein crystals *J. Appl. Crystallogr.* **22** 115–8
[39] Pusey M L and Nadarajah A 2002 A model for tetragonal lysozyme crystal nucleation and growth *Cryst. Growth Design* **2** 475–83
[40] Pusey M L and Naumann R 1986 Growth kinetics of tetragonal lysozyme crystals *J. Cryst. Growth* **76** 593–9
[41] Pusey M L, Witherow W and Naumann R 1988 Preliminary investigations into solutal flow about growing tetragonal lysozyme crystals *J. Cryst. Growth* **90** 105–11
[42] Ramkrishna D 2000 *Population Balances—Theory and Applications to Particulate Systems in Engineering* (San Diego, CA: Academic)
[43] Rawlings J B, Miller S M and Witkowski W R 1993 Model identification and control of solution crystallization process—a review *Indust. Eng. Chem. Res.* **32** 1275–96
[44] Rohani S and Bourne J R 1990 Self-tuning control of crystal size distribution in a cooling batch crystallizer *Chem. Eng. Sci.* **12** 3457–66
[45] Rosenberger F 1996 Protein crystallization *J. Cryst. Growth* **166** 40–54
[46] Rosenberger F, Howard S B, Sowers J W and Nyce T A 1993 Temperature dependence of protein solubility determination and application to crystallization in x-ray capillaries *J. Cryst. Growth* **129** 1–12
[47] Rosenberger F and Meehan E J 1988 Control of nucleation and growth in protein crystal growth *J. Cryst. Growth* **90** 74–8
[48] Rosenberger F, Vekilov P G, Muschol M and Thomas B R 1996 Nucleation and crystallization of globular proteins—what we know and what is missing *J. Cryst. Growth* **168** 1–27
[49] Saridakis E and Chayen N E 2003 Systematic improvement of protein crystals by determining the supersolubility curves of phase diagrams *Biophys. J.* **84** 1218–22
[50] Sazaki G, Kurihara K, Nakada T, Miyashita S and Komatsu H 1996 A novel approach to the solubility measurement of protein crystals by two-beam interferometry *J. Cryst. Growth* **169** 355–60
[51] Schall C A, Riley J S, Li E, Arnold E and Wiencek J M 1996 Application of temperature control strategies to the growth of hen egg-white lysozyme crystals *J. Cryst. Growth* **165** 299–307
[52] Shi D, El-Farra N H, Li M, Mhaskar P and Christofides P D 2005 Predictive control of particle size distribution in particulate processes *Chem. Eng. Sci.* at press
[53] Togkalidou T, Braatz R D, Johnson B K, Davidson O and Andrews A 2001 Experimental design and inferential modeling in pharmaceutical crystallization *AIChE J.* **47** 160–8
[54] Vekilov P G and Chernov A A 2002 The physics of protein crystallization *Solid State Phys.—Adv. Res. Applications* **57** 1–147
[55] Vekilov P G and Rosenberger F 1996 Dependence of lysozyme growth kinetics on step sources and impurities *J. Cryst. Growth* **158** 540–51
[56] Ward K B, Zuk W M, Perozzo M A, Walker M A, Birnbaum G I, Kung W, Cavaliere A, Uffen D R and Scholaert H 1992 Dynamic telerobotic control of crystallization experiments *J. Cryst. Growth* **122** 235–41
[57] Wiencek J M 1999 New strategies for protein crystal growth *Annu. Rev. Biomed. Eng.* **1** 505–34
[58] Xie W, Rohani S and Phoenix A 2001 Dynamic modeling and operation of a seeded batch cooling crystallizer *Chem. Eng. Commun.* **187** 229–49
[59] Zhang G P and Rohani S 2003 On-line optimal control of a seeded batch cooling crystallizer *Chem. Eng. Sci.* **58** 1887–96